Dynamics of Synthetic Membraneless Organelles in Microfluidic Droplets

Miriam Linsenmeier, Marie R. G. Kopp, Fulvio Grigolato, Leonidas Emmanoulidis, Dany Liu, Dominik Zürcher, Maria Hondele, Karsten Weis, Umberto Capasso Palmiero, and Paolo Arosio*

Abstract: *Cells can form membraneless organelles by liquid–liquid phase separation. As these organelles are highly dynamic, it is crucial to understand the kinetics of these phase transitions. Here, we use droplet-based microfluidics to mix reagents by chaotic advection and observe nucleation, growth, and coarsening in volumes comparable to cells (pL) and on timescales of seconds. We apply this platform to analyze the dynamics of synthetic organelles formed by the DEAD-box ATPase Dhh1 and RNA, which are associated with the formation of processing bodies in yeast. We show that the timescale of phase separation decreases linearly as the volume of the compartment increases. Moreover, the synthetic organelles coarsen into one single droplet via gravity-induced coalescence, which can be arrested by introducing a hydrogel matrix that mimics the cytoskeleton. This approach is an attractive platform to investigate the dynamics of compartmentalization in artificial cells.*

Proteins and nucleic acids can form dynamic membraneless compartments by liquid–liquid phase separation (LLPS).[1–3] These protein-rich condensates have been observed in many different species and recruit molecules associated with a variety of crucial cellular functions, including RNA metabolism and stress signaling.[3]

While there has been significant progress over the past few years in describing biological systems undergoing LLPS,[4] the dynamics of these processes remain largely unexplored, despite the observations that dynamics play a key role in LLPS.[3,5] For example, membraneless organelles resulting from LLPS exhibit rapid internal mixing, fast exchange with the external environment, and transform rapidly via a constant flux of molecules.[3] Moreover, cells are intrinsically out-of-equilibrium systems in which the achievement of thermodynamic equilibrium is prevented by biochemical reactions.[6–8] In this context, kinetics and nucleation barriers[9] define the behavior of the system in addition to thermodynamics. Consequently, the dynamics of assembly and disassembly of the compartments is crucial to understand the mechanisms developed by cells to react to environmental changes and to control the composition, stability, and size distribution of these organelles. Moreover, misregulation of organelle dissolution has been linked to disease.[10] Despite the essential role of dynamics in living organisms, the mechanisms of assembly and disassembly of these membraneless organelles remain largely unexplored, in part due to the lack of available experimental tools to study the dynamics of the phase transitions on short time scales.

Droplet microfluidic technology[11,12] is emerging as an attractive approach to investigate protein phase transition[13,14] and aggregation,[15,16] as well as to generate artificial cell compartmentalization and synthetic organelles.[17–19] Herein, we demonstrate that droplet microfluidic approaches are powerful tools to probe the dynamics of biomolecular LLPS in well-defined microcompartments generated by segmented flow microfluidic devices capable of controlling multiphase flow. With these microfluidic mixers and reactors, we rapidly mixed reagents via chaotic advection and observe nucleation, growth, and coarsening events in volumes comparable to cells (pL) on timescale of seconds. Moreover, the compartmentalization of solutions in droplets facilitates improved control over the system, as phase transitions can be monitored from well-defined initial conditions and with limited interactions with interfaces, which may significantly alter phase transitions. Importantly, monitoring phase-transition events in microcompartments provides the unique opportunity to investigate the effect of confinement in volumes comparable to cells.[20]

Here, we exploited our microfluidics technology to investigate the dynamics of LLPSs associated with an in vitro model system of a biological membraneless organelle. In particular, we probed the dynamics of synthetic organelles formed by the DEAD-box ATPase Dhh1 and RNA.

Dhh1 is an RNA-binding protein that is associated with the formation of processing bodies in *Saccharomyces cerevisiae* during stress conditions.[21] Recently, molecular modulators that control the reversible phase separation of Dhh1 have been identified.[21–23] Specifically, it has been shown that the addition of ATP and RNA increases intermolecular interactions[21] and induces the formation of protein-rich droplets that exhibit liquid-like behavior (Figure 1 A), as revealed by microscopy and fluorescence recovery after photobleaching (FRAP, Supporting Information, Figure S1).

[*] M. Linsenmeier, M. R. G. Kopp, F. Grigolato, D. Liu, D. Zürcher,
Dr. U. Capasso Palmiero, Prof. Dr. P. Arosio
Department of Chemistry and Applied Biosciences,
Institute for Chemical and Bioengineering, ETH Zürich
8093 Zurich (Switzerland)
E-mail: paolo.arosio@chem.ethz.ch

Dr. M. Hondele, Prof. Dr. K. Weis
Department of Biology, Institute of Biochemistry, ETH Zürich
8093 Zurich (Switzerland)

Dr. L. Emmanoulidis
Institute of Molecular Biology and Biophysics,
Department of Biology, ETH Zurich, 8093 Zurich (Switzerland)

📱 Supporting information and the ORCID identification number(s) for
ⓘ the author(s) of this article can be found under:
https://doi.org/10.1002/anie.201907278.
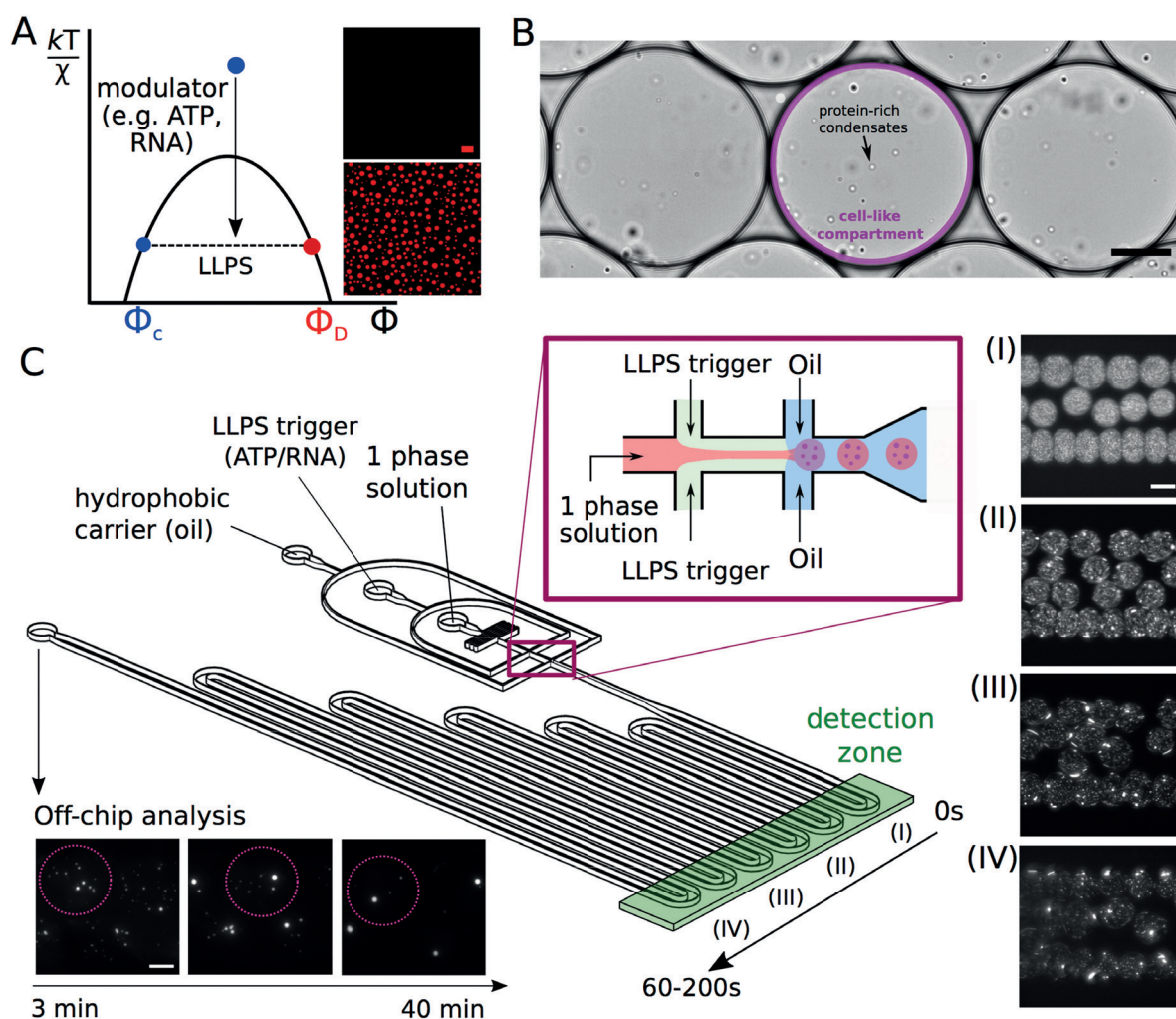
Figure 1. Dynamics of liquid–liquid phase separation (LLPS) observed in a droplet microfluidic device. A) Several molecular modulators control the phase diagram and the LLPS of the DEAD-box ATPase Dhh1, including ATP and RNA. B) Representative bright-field images showing the formation of synthetic organelles of Dhh1 and RNA in water-in-oil emulsions, mimicking cell-like compartments (scale bar: 100 μm). C) Schematic overview of the droplet microfluidic device. In the first junction, LLPS is triggered by mixing a one-phase protein solution of Dhh1 with ATP and polyU. In the second junction, the solution is compartmentalized into a water-in-oil emulsion. The kinetics of LLPS were observed on-chip by acquiring images at 12 different positions in the detection zone (highlighted in green). Four representative images at different positions are shown on the right column (scale bar: 100 μm). Kinetics were further followed off-chip by transferring the compartments in glass capillaries, in which LLPS was monitored over 20–40 minutes. Dot circles indicate individual compartments (scale bar: 20 μm).

This system represents an ideal model to investigate the dynamics of the LLPS process. To this end, we induced the formation of synthetic organelles by rapidly mixing the protein solution with the molecular triggers (ATP, RNA) on a droplet microfluidic platform (Figure 1B). A schematic drawing of the device is shown in Figure 1C. The device consists of two junctions and three inlets: i) the hydrophobic carrier fluid of the microcompartments, which is an HFE-7500 oil (Acota Limited) containing 0.2% surfactant (Pico-Surf 1, Sphere Fluidics, Cambridge, UK); ii) the protein solution with 5 μM of recombinantly expressed and purified mCherry-tagged Dhh1 diluted in 30 mM HEPES-KOH, pH 7.4, 2 mM MgCl$_2$, and 200 mM KCl; iii) the solution containing the triggers that initiate LLPS (50 mM ATP and 0.2 mg mL^{-1} polyU in 2 mM MgCl$_2$ and 30 mM HEPES-KOH, pH 7.4, Figure 1C).

At the first junction, the protein solution is mixed with ATP and polyU to produce a final solution of 16.7 mM ATP, 0.06 mg mL^{-1} polyU, 133 mM KCl, and 3.3 μM Dhh1. At the second junction, this solution is compartmentalized into a water-in-oil emulsion by the carrier fluid. The water solution inside the droplets is mixed by chaotic advection on a sub-millisecond time scale,[24] thereby guaranteeing rapid mixing and well-defined initial conditions for the phase transition. Moreover, the droplet microfluidic technique generates compartments with monodisperse size distributions (Supporting Information, Figure S2), which can be easily controlled by changing the volumetric flow rates of the inlet solutions and the diameter of the nozzle. In our experiments, we created cell-like compartments of different volumes ranging from 5 to 80 pL by varying the diameter of the nozzle from 30 μm to 150 μm. The water-in-oil emulsion was

stabilized by a polyfluorinated block-copolymer surfactant, chosen to minimize the interactions with proteins, which could potentially modulate the protein phase transition.[25] Moreover, our setup avoids contacts between the protein and the surfactant before encapsulation.

After their formation, the cell-like compartments flow in the channel, where they are imaged at 12 different positions, corresponding to 12 different time points in a short time interval varying from 2 to 60–200 s (Figure 1 C).

Initially, the cell-like compartments exhibit a homogenous intensity distribution corresponding to the soluble monomeric proteins. Over time, the fluorescence profiles become more granular and gradually distinct droplets appear (images I–IV), corresponding to the formation of the protein-RNA droplets. At the end of the channel, the cell-like compartments can be collected in glass capillaries and monitored over longer time scales ranging from several minutes to several hours. During this timescale, we observed merging of the protein–RNA condensates into one single droplet within each compartment (Figure 1 C).

We first applied the droplet microfluidic platform to measure the kinetics of phase separation within cell-like compartments of varying volumes of 6.3 ± 0.5, 12.3 ± 4.6, 38.2 ± 1.5, and 79.7 ± 7.6 pL (Figure 2 and Supporting Information, Figure S3).

We calculated the total amount of protein recruited into the protein-rich droplets by analyzing the fraction of the high-intensity pixels in the intensity distribution (Figure 2 A and Supporting Information, Eq. (S1)–(S2) and Figures S4 and S5).

Our results show that the rate of formation of the synthetic organelles increases with increasing compartment volume (Figure 2 B). We estimated the corresponding characteristic times of phase separation (τ) by fitting the time evolution of the high and low intensity pixels at different confinement volumes (Figure 2 B and Supporting Information, Figure S6). The phase-separation kinetics can be described with a simplified model based on a second-order process (Supporting Information, Eq. (S3)–(S5)). We observed that the characteristic time of phase separation τ scales linearly with the confinement volume (Figure 2 C).

The linear dependence of the characteristic time τ on the system size V (Figure 2 C and Supporting Information, Figure S6) would be consistent with the presence of rare events characterized by a low reaction rate r ($\tau = r^{-1} V^{-1}$). This behavior has been observed with rare nucleation processes associated with other types of protein self-assembly, such as crystallization and amyloid formation.[15] Our results thus suggest that the formation of synthetic organelles may follow similar nucleation and growth mechanisms, in which nucleation rates scale linearly with the volume of the compartment. Moreover, the findings further imply that the dynamics of membraneless organelles could depend on the cell type or the subcellular compartment in which they are generated.
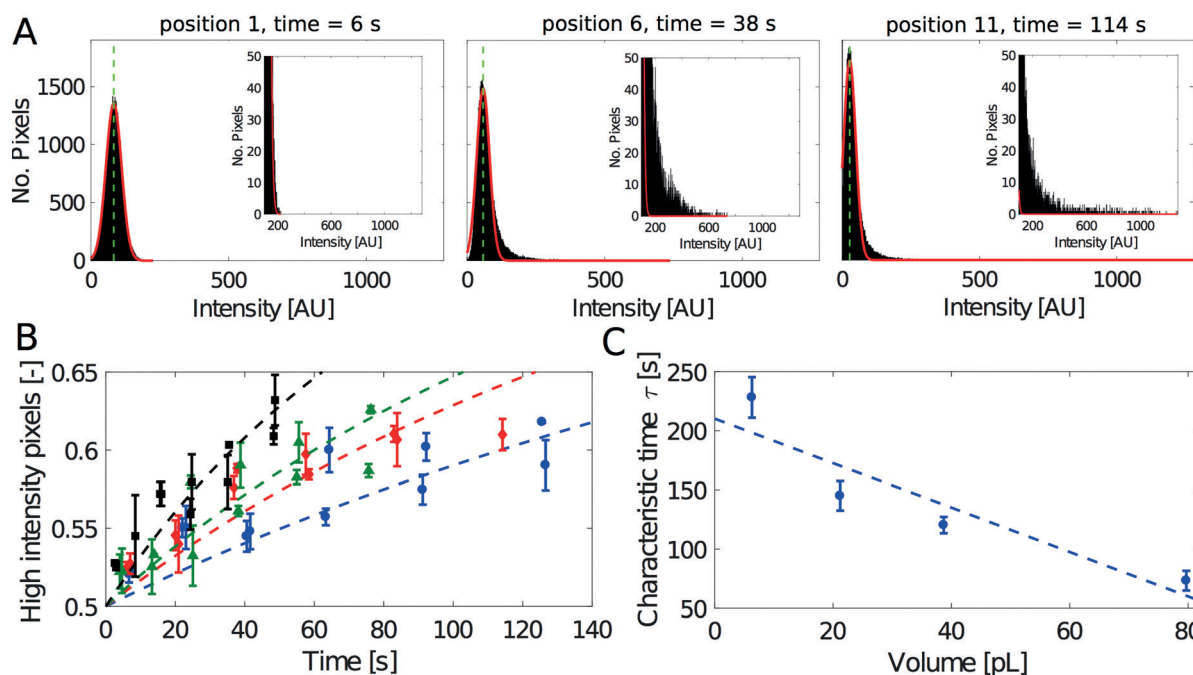
Figure 2. Kinetics of liquid–liquid phase separation. A) Intensity distributions of individual compartments at positions 1 (6 s), 6 (38 s). and 11 (114 s). The red line represents the Gaussian fitting and the green dashed line indicates the mean intensity, which divides the distribution into low and high intensity pixels. The inserts show the increase in the tail of the intensity distributions over time. B) Number of high intensity (HI) pixels over time, normalized by the total area of the distribution. This value is proportional to the total amount of protein recruited into the protein–RNA droplets. Different colors correspond to different compartment volumes: 6.3 ± 0.5 (blue), 21.3 ± 4.6 (red), 38.2 ± 1.5 (green), and 79.7 ± 7.6 pL (black). Symbols represent experimental data and dashed lines are model fits (see Eq. (S1),(S2) in the Supporting Information). C) Characteristic time τ of phase transition as a function of the confinement volume (V) evaluated according to Equations (S3)–(S5) in the Supporting Information; $R^2 = 0.83$.
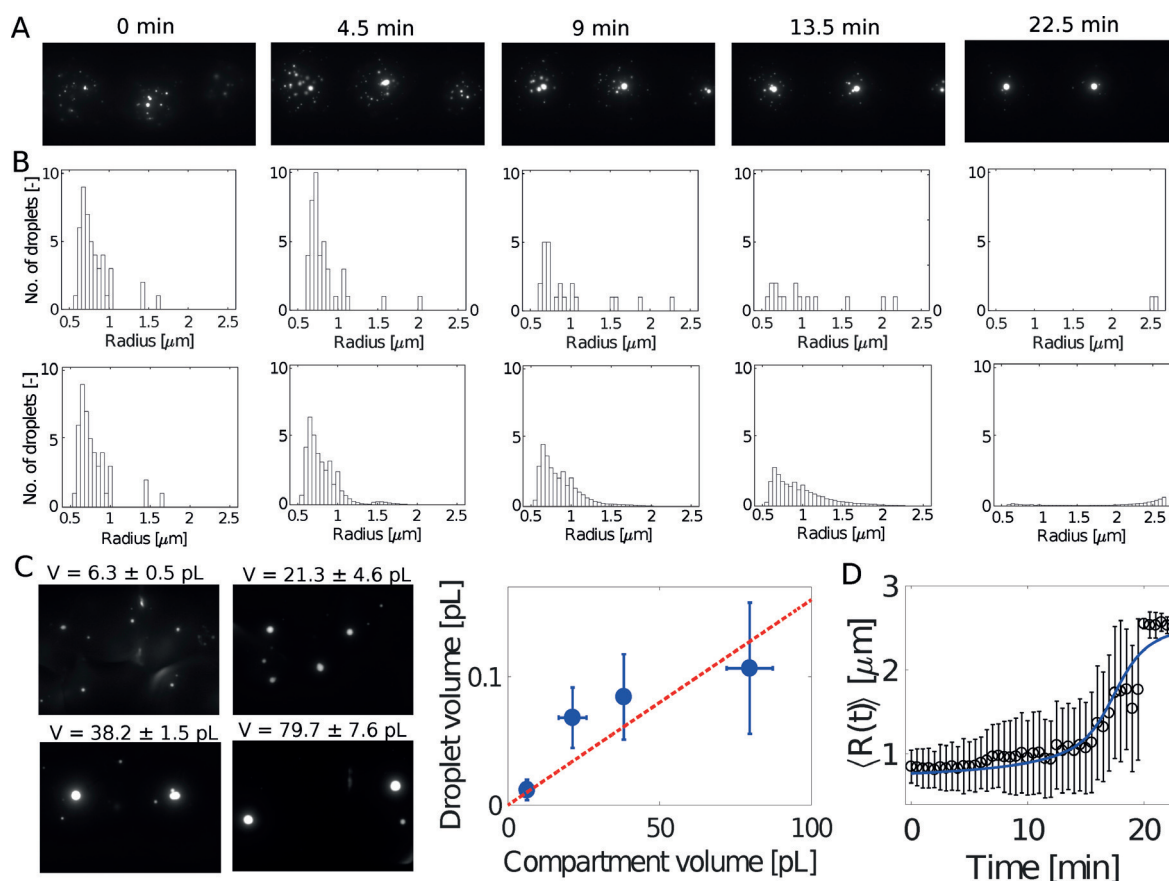
Figure 3. Coarsening of protein-rich droplets over time. A) Images of individual compartments showing the fusion of protein–RNA condensates into one single droplet over 25 minutes. B) Corresponding experimentally measured (top row) and simulated (bottom row) size distributions of the droplets, showing the shift from a polydisperse distribution with numerous droplets to a monodisperse solution with one single droplet in each compartment. Simulations are based on gravity-induced coalescence (Supporting Information). C) Volumes and images of the final droplets generated in compartments of different volumes from solutions at constant protein concentrations. The average droplet volume increases with increasing confinement volume, $R^2 = 0.57$. D) Model simulations based on gravity-induced coalescence (continuous blue line) are compatible with the time evolution of both the average radius and the full size distributions (panel (B)).

We next quantified the kinetics of coarsening of the protein-rich droplets over time by imaging the compartments after collecting them in glass capillaries. We observed that in each compartment multiple droplets coalesce over time into one single droplet (Figure 3 A,B and Supporting Information, Figure S7).

The volume of the final single droplet scales linearly with the volume of the compartment (Figure 3 C) and therefore with the total amount of initial monomeric protein, since the experiments were performed at constant protein concentration. This result is consistent with findings observed in vivo with *Caenorhabditis elegans* embryos, in which the size of the nucleolus scales directly with the cell size.[20]

To gain insight into the mechanisms of droplet coarsening, we quantified the kinetic rate of droplet coarsening by analyzing the time evolution of the average size of the droplets extracted from the images acquired over 20 min (Figure 4 B). Model simulations based on either diffusion-limited Ostwald ripening (DLO) or Brownian-motion-induced coalescence (BMC) are not consistent with our experimental data (Supporting Information, Figures S8 and S9), suggesting that Ostwald ripening and Brownian motion are not the main mechanisms underlying droplet coarsening.

Given the micron-size of the droplets and the absence of cytoskeleton-like structures in our compartments, it is expected that droplets can sediment over time, thereby
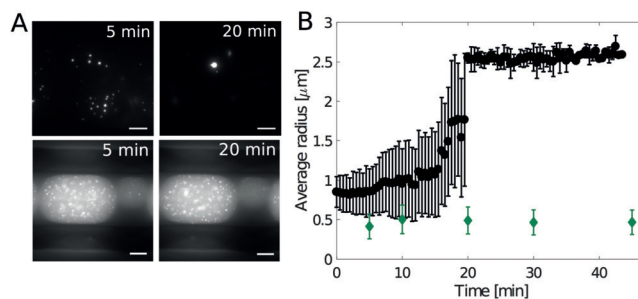
Figure 4. Hydrogels prevent coarsening over time. A) Droplet coarsening in the absence (top panels) and presence (bottom panels) of a hydrogel matrix. Scale bar: 20 µm. B) Average droplet radius over time in the absence (black circles) and presence (green diamonds) of a hydrogel.

affecting the collision events leading to droplet coarsening. We analyzed the effect of sedimentation by considering gravity-induced collision kernels in the Smoluchowski population balance equation that describes droplet coarsening (Supporting Information). Approximate solution of this master equation leads to the following equation describing the time evolution of the average droplet radius $\langle R(t) \rangle$:[26]

$$\frac{R_0}{\langle R(t) \rangle} = 1 - \frac{2t}{3t_g} \qquad (1)$$

where R_0 is the initial average droplet radius and t_g is the characteristic gravitational settling time given by $t_g = \frac{4R_0}{3\phi v_{g,0}E_0}$, where $v_{g,0}$ is the droplet gravitational settling velocity, ϕ is the droplet volume fraction, and $E_0 = 1$ is the characteristic collision efficiency (Supporting Information).[26]

Both approximate and numerical solutions of the master equation with kernels based on gravity-induced coalescence are in agreement not only with the increase of the average radius over time (Figure 3 D) but also with the time evolution of the full size distribution (Figure 3 B). Moreover, the overall timescale of coalescence (about 20–25 min) is consistent with the characteristic gravitational settling time (22.2 min). Overall, this kinetic analysis suggests that gravity-induced coalescence is the dominating mechanism responsible for droplet coarsening in our system.

It has previously been shown that nucleoli in *Xenopus laevis* oocytes coalesce upon deletion of the actin cytoskeleton.[27] Our observation of droplet coalescence via gravitation is consistent with this data, given that our compartments lack cytoskeleton-like structures. However, the presence of a filamentous network can highly affect droplet growth and coarsening.[28]

The effects of cytoskeleton-like structures on droplet coarsening can be easily tested in our droplet microfluidic platform. We demonstrated this possibility by assembling a polydimethylacrylamide (PDMA) hydrogel matrix inside our compartments (Figure 4 and Supporting Information, Figure S10).

In the absence of the hydrogel, the droplets coalesced within 20 minutes (Figure 4 A and Supporting Information, Figure S11, upper panels). In contrast, in the presence of the hydrogel, the coalescence of the droplets was prevented and their coarsening arrested when an average radius of 0.46 ± 0.03 µm was reached (Figure 4 A,B and Supporting Information, Figure S11, lower panels).

Overall, these results illustrate how the droplet microfluidic set-up represents an attractive model system to investigate the dynamics of membraneless compartments on a time scale of seconds as well as the partitioning of different biomolecules in space in cell-like model systems. Our analysis shows that the timescale of phase separation decreases linearly as the compartment volume increases, indicating that the dynamics of membraneless organelles could change within different cellular sub-compartments.

We envision applications of this platform for the analysis of the effect of different modulators on the assembly and disassembly of biomolecular condensates, in both the absence and presence of cytoskeleton-like structures.

We anticipate that this microfluidic approach is a promising strategy to probe the dynamics of compartmentalization not only for simple artificial systems, but also for complex cellular models. To this aim, the method can be further adapted to incorporate biologically relevant phospholipids as well as cytoskeleton polymers, such as tubulin and actin. Moreover, the combination of experimental data with model analysis could allow the investigation of more complex reaction networks.[29]

Conflict of interest

The authors declare no conflict of interest.

[1] C. P. Brangwynne, C. R. Eckmann, D. S. Courson, A. Rybarska, C. Hoege, J. Gharakhani, F. Jülicher, A. A. Hyman, *Science* **2009**, *324*, 1729–1732.

[2] M. Kato, T. W. Han, S. Xie, K. Shi, X. Du, L. C. Wu, H. Mirzaei, E. J. Goldsmith, J. Longgood, J. Pei, et al., *Cell* **2012**, *149*, 753–767.

[3] S. F. Banani, H. O. Lee, A. A. Hyman, M. K. Rosen, *Nat. Rev. Mol. Cell Biol.* **2017**, *18*, 285–298.

[4] D. M. Mitrea, J. A. Cika, C. B. Stanley, A. Nourse, P. L. Onuchic, P. R. Banerjee, A. H. Phillips, C. G. Park, A. A. Deniz, R. W. Kriwacki, *Nat. Commun.* **2018**, *9*, 1–13.

[5] J. Berry, S. C. Weber, N. Vaidya, M. Haataja, C. P. Brangwynne, *Proc. Natl. Acad. Sci. USA* **2015**, *112*, E5237–E5245.

[6] B. A. Grzybowski, W. T. S. Huck, *Nat. Nanotechnol.* **2016**, *11*, 585–592.

[7] P. R. Banerjee, A. N. Milin, M. M. Moosa, P. L. Onuchic, A. A. Deniz, *Angew. Chem. Int. Ed.* **2017**, *56*, 11354–11359; *Angew. Chem.* **2017**, *129*, 11512–11517.

[8] C. A. Weber, D. Zwicker, F. Jülicher, C. F. Lee, *Rep. Prog. Phys.* **2019**, *82*, 064601.

[9] T. Khan, T. S. Kandola, J. Wu, S. Venkatesan, E. Ketter, J. J. Lange, A. Rodríguez Gama, A. Box, J. R. Unruh, M. Cook, et al., *Mol. Cell* **2018**, *71*, 155–168.

[10] A. Patel, H. O. Lee, L. Jawerth, S. Maharana, M. Jahnel, M. Y. Hein, S. Stoynov, J. Mahamid, S. Saha, T. M. Franzmann, et al., *Cell* **2015**, *162*, 1066–1077.

[11] X. Casadevall i Solvas, A. DeMello, *Chem. Commun.* **2011**, *47*, 1936–1942.

[12] J. J. Agresti, E. Antipov, A. R. Abate, K. Ahn, A. C. Rowat, J.-C. Baret, M. Marquez, A. M. Klibanov, A. D. Griffiths, D. A. Weitz, *Proc. Natl. Acad. Sci. USA* **2010**, *107*, 4004–4009.

[13] J. U. Shim, G. Cristobal, D. R. Link, T. Thorsen, Y. Jia, K. Piattelli, S. Fraden, *J. Am. Chem. Soc.* **2007**, *129*, 8825–8835.

[14] B. Zheng, L. S. Roach, R. F. Ismagilov, *J. Am. Chem. Soc.* **2003**, *125*, 11170–11171.

[15] T. P. J. Knowles, D. A. White, A. R. Abate, J. J. Agresti, S. I. A. Cohen, R. A. Sperling, E. J. De Genst, C. M. Dobson, D. A. Weitz, *Proc. Natl. Acad. Sci. USA* **2011**, *108*, 14746–14751.

[16] T. W. Herling, A. Levin, K. L. Saar, C. M. Dobson, T. P. J. Knowles, *Lab Chip* **2018**, *18*, 999–1016.

[17] N. N. Deng, W. T. S. Huck, *Angew. Chem. Int. Ed.* **2017**, *56*, 9736–9740; *Angew. Chem.* **2017**, *129*, 9868–9872.

[18] M. Ugrinic, A. Zambrano, S. Berger, S. Mann, T.-Y. D. Tang, A. DeMello, *Chem. Commun.* **2018**, *54*, 287–290.

[19] B. Drobot, J. M. Iglesias-Artola, K. Le Vay, V. Mayr, M. Kar, M. Kreysing, H. Mutschler, T. Y. D. Tang, *Nat. Commun.* **2018**, *9*, 3643.

[20] S. C. Weber, C. P. Brangwynne, *Curr. Biol.* **2015**, *25*, 641–646.

[21] C. F. Mugler, M. Hondele, S. Heinrich, R. Sachdev, P. Vallotton, A. Y. Koek, L. Y. Chan, K. Weis, *eLife* **2016**, *5*, e18746.

[22] R. Sachdev, M. Hondele, M. Linsenmeier, P. Vallotton, C. F. Mugler, P. Arosio, K. Weis, *eLife* **2019**, *8*, e41415.

[23] L. Faltova, A. M. Küffner, M. Hondele, K. Weis, P. Arosio, *ACS Nano* **2018**, *12*, 9991–9999.

[24] H. Song, M. R. Bringer, J. D. Tice, C. J. Gerdts, R. F. Ismagilov, *Appl. Phys. Lett.* **2003**, *83*, 4664–4666.

[25] E. Grignaschi, G. Cereghetti, F. Grigolato, M. R. G. Kopp, S. Caimi, L. Faltova, S. Saad, M. Peter, P. Arosio, *J. Biol. Chem.* **2018**, *293*, 11424–11432.

[26] H. Wang, R. H. Davis, *J. Colloid Interface Sci.* **1993**, *159*, 108–118.

[27] M. Feric, C. P. Brangwynne, *Nat. Cell Biol.* **2013**, *15*, 1253–1259.

[28] R. W. Style, T. Sai, N. Fanelli, M. Ijavi, K. Smith-Mannschott, Q. Xu, L. A. Wilen, E. R. Dufresne, *Phys. Rev. X* **2018**, *8*, 11028.

[29] P. Arosio, T. C. T. Michaels, S. Linse, C. Månsson, C. Emanuelsson, J. Presto, J. Johansson, M. Vendruscolo, C. M. Dobson, T. P. J. Knowles, *Nat. Commun.* **2016**, *7*, 10948.